

Strong field effects on emission line profiles: Kerr black holes and warped accretion disks

Yan Wang and Xiang-Dong Li

Department of Astronomy, Nanjing University, Nanjing 210093, China

Key Laboratory of Modern Astronomy and Astrophysics (Nanjing University), Ministry of Education, Nanjing 210093, China

ABSTRACT

If an accretion disk around a black hole is illuminated by hard X-rays from non-thermal coronae, fluorescent iron lines will be emitted from the inner region of the accretion disk. The emission line profiles will show a variety of strong field effects, which may be used as a probe of the spin parameter of the black hole and the structure of the accretion disk. In this paper we generalize the previous relativistic line profile models by including both the black hole spinning effects and the non-axisymmetries of warped accretion disks. Our results show different features from the conventional calculations for either a flat disk around a Kerr black hole or a warped disk around a Schwarzschild black hole by presenting, at the same time, multiple peaks, rather long red tails and time variations of line profiles with the precession of the disk. We show disk images as seen by a distant observer, which are distorted by the strong gravity. Although we are primarily concerned with the iron K-shell lines in this paper, the calculation is general and is valid for any emission lines produced from a warped accretion disk around a black hole.

1. Introduction

Accretion power serves as an important source of energy in astrophysics, especially in galactic X-ray binaries (XRBs) and active galactic nuclei (AGNs). In these systems, black holes (BHs) are the possible candidates for the central accreting compact objects. Accretion onto both stellar-mass black holes in XRBs and supermassive black holes ($10^6 - 10^9 M_\odot$) in AGNs usually proceeds through an accretion disk, which may be truncated at the inner most stable circular orbit (ISCO) because of the general relativistic effect of black hole. Due to viscosity, plasma elements in the disk gradually spiral inwards to the black hole while losing their angular momenta until reaching the ISCO; they then plunge into the black hole, if there is no external force acting on them.

The quasi-thermal spectra of the black hole accretion disks are relatively cold, which peak at optical/UV band in AGNs and soft X-ray band in XRBs (Frank et al. 2002). If point-like hot coronae, above and below the center of the accretion disk (as in the lamp-post model (Matt et al. 1991)), illuminate the inner region of the disk by hard X-ray photons yielded via thermal Comptonization, iron atoms photoelectrically absorb the incident hard X-ray photons, then emit iron K-shell photons (centered at $6.40 - 6.97$ keV, depending on the ionization state) through the fluorescent mechanism. Iron K-shell lines may be the strongest emission lines in the X-ray observations of XRBs (Barr et al. (1985), Miller et al. (2002a) for Cygnus X-1; Miller et al. (2002b), Miniutti et al. (2004), Rossi et al. (2005) for XTE J1650-500) and AGNs (Tanaka et al. (1995), Wilms et al. (2001), Brenneman & Reynolds (2006), Miniutti et al. (2007) for the Seyfert-1 MCG-6-30-15, the most important source to date). Observations suggest that some two-horn broadened iron K-shell lines

originate from the innermost area of the accretion disk. The iron lines could be a powerful tool to study the strong gravity within a few gravitational radius $r_g = GM/c^2$ and a probe of the black hole spin parameter (see reviews by Reynolds & Nowak (2003) and Miller (2007)).

Fabian et al. (1989) modeled the relativistic line profile from a standard thin disk (see Shakura & Sunyaev (1973) for Newtonian disk model; Novikov & Thorne (1973) and Page & Thorne (1974) for general relativistic effects) orbiting around a Schwarzschild black hole. Laor (1991) and Bromley et al. (1997) calculated the line profile from a standard thin disk orbiting around an extreme Kerr black hole. Fanton et al. (1997) calculated the line profile from a standard thin disk orbiting around a Kerr black hole with spin parameter $a = cJ/GM$ (where J is the angular momentum and M is the mass of the black hole) as a free parameter, in their calculation the complication of computing azimuthal angle ϕ has been avoided due to the axisymmetry of both the Kerr metric and the accretion disk. Thereafter, the line profiles from accretion disks with different structures have been investigated: for a warped accretion disk orbiting around a Schwarzschild black hole (Hartnoll & Blackman 2000; Wu et al. 2008), and for a flat accretion disk with spiral patterns orbiting around a nonrotating black hole (Hartnoll & Blackman 2002) or a rotating black hole (Karas et al. 2001). In these calculations, the accretion disks are optically thick and geometrically thin; furthermore it was assumed that the plasma elements within ISCO contribute little to the line profiles, because they are hot and almost fully ionized (Young et al. 1998; Brenneman & Reynolds 2006). In contrast with the thin disk, Wu & Wang (2007) explored the role of disk self-shadowing effect due to significant geometrical thickness. Fuerst & Wu (2007) investigated the influence of geometrical thickness of relativistic accretion torus on the line profiles.

It is interesting to model the relativistic iron K-shell lines emerging from the warped disks orbiting around Kerr black holes. Bardeen & Petterson (1975) showed that for Kerr black holes the dragging of inertial frames can lead to coupling between the spin of the black hole and the orbital angular momentum of the disk, and that the component of the viscous torque, which is in the disk plane and perpendicular to the line of nodes, will tend to force the inner part of the disk to lie on the equatorial plane of the Kerr black hole. Nevertheless, misalignment of the inner part of the disk may take place even in the presence of dissipation. Demianski & Ivanov (1997) and Ivanov & Illarionov (1997) showed that the misaligned disk adopts a steady warped shape in which the tilt angle is an oscillatory function of radius. Lubow et al. (2002) considered the time evolution of the warped disk under the condition that the warping propagates in a wave like manner, and concluded that, in low-viscosity disk around a Kerr black hole, the inner parts of the disk are not necessarily aligned with the black hole. Warping may be induced by non-axisymmetric radiation pressure (Pringle 1996; Maloney et al. 1998) or tidal interaction (Terquem & Bertout 1993; Larwood et al. 1996). In observations, evidence of warped disks in XRB includes the 35-days periodic variation of X-ray flux of Her X-1 (Tananbaum et al. 1972; Katz 1973) and the precessing relativistic jet in SS 433 (Margon 1984); for AGNs disk warping can explain the radial dependence of declination between high-velocity maser and systemic maser in NGC 4258 (Miyoshi et al. 1995; Martin 2008) and the misalignment between the angular momentum of the radio jets and the host galactic disks (Kinney et al. 2000; Schmitt et al. 2002).

The motivation of this work is multiple. Firstly, the iron K-shell lines carry the information about the spacetime around a rotating black hole; fitting line profiles from the observational data with better spectral resolution and signal-noise ratio by more realistic disk line models may provide more reliable estimations of the spin parameter of the black hole (Abramowicz et al. 2010), and distinguish the warping effects on line profiles from others. Secondly, the disk lines may be used to diagnose the geometry and kinematics of the disk itself, and provide observational signatures for the existence and characteristics (magnitude, twist-free or twisted) of the warping.

The paper is organized as follows. In Sec. 2 we review the properties of photon trajectories in the Kerr

spacetime, and summarize the relevant equations needed in our calculation. Next, we describe in Sec. 3.1 the geometric formalism for the warped disk and in Sec. 3.2 the kinematic structure. These considerations are employed in Sec. 4, where we show our main results, including the emission line profiles and the images of the warped disk around a Kerr black hole observed from a distant place. We summarize the main results and discuss their possible implications in Sec. 5. To allow the main ideas of the paper to be as clear as possible, several sets of details have been relegated to appendix A, in which we give the detailed procedure for deriving the expression of the ratio g for the warped disk. The relativistic calculations presented in this paper use the notational conventions of the text by Misner et al. (1973); in particular we use $c = G = 1$.

2. Photon trajectories in the Kerr spacetime

When calculating the relativistic line profiles, one needs to trace the trajectories of the photons in the Kerr spacetime. In the standard Boyer-Lindquist coordinates, the Kerr metric can be written as

$$ds^2 = -\Sigma\Delta A^{-1}dt^2 + \sin^2\theta A\Sigma^{-1}(d\phi - \omega dt)^2 + \Sigma\Delta^{-1}dr^2 + \Sigma d\theta^2, \quad (1)$$

where

$$\Sigma = r^2 + a^2 \cos^2\theta, \quad (2)$$

$$\Delta = r^2 + a^2 - 2Mr, \quad (3)$$

$$A = (r^2 + a^2)^2 - a^2 \sin^2\theta \Delta = \Sigma(r^2 + a^2) + 2Ma^2r \sin^2\theta, \quad (4)$$

$$\omega = 2aMrA^{-1}. \quad (5)$$

This metric contains two parameters, the mass of the black hole M and the specific angular momentum or the spin parameter $a = J/M$. The greater root $r_+ = M + \sqrt{M^2 - a^2}$ of $\Delta = 0$ corresponds to the event horizon which is an one-way membrane in the Kerr spacetime. We notice that the right-hand-sides of Eqs. 2-5 are always positive outside the event horizon. The dragging of inertial frame forbids any observer remaining static within the static limit $r_{\text{sl}}(\theta) = M + \sqrt{M^2 - a^2 \cos^2\theta}$.

Given a spacetime background, the motion of a photon obeys the null geodesic equation $\nabla_{\mathbf{p}} \cdot \mathbf{p} = 0$, where \mathbf{p} is the 4-momentum of the photon and $\nabla_{\mathbf{p}}$ is the directional derivative operator along \mathbf{p} . This is a set of second-order ordinary differential equation, which can be solved in principle by the Runge-Kutta method with given initial position and momentum of the photon. Alternatively, in Kerr spacetime one can take advantage of its axisymmetric property (the corresponding constants of motion include the energy of the photon E , the angular momentum along the spin axis L_z , and the norm of the 4-momentum δ), and solve the trajectory of photon in the equatorial plane by the Lagrangian approach. For the general null geodesics in the Kerr spacetime, Carter (1968) demonstrated the separability of the Hamilton-Jacobi equation and discovered the existence the fourth constant of motion (i.e. Carter constant \mathcal{Q}). To obtain the equations governing the motion of the photons, one can take the partial derivatives of the Hamilton's principle function

$$S = \frac{1}{2}\delta\lambda - Et + L_z\phi + \int^r \frac{\sqrt{R(r)}}{\Delta} dr + \int^\theta \sqrt{\Theta(\theta)} d\theta, \quad (6)$$

with respect to E , L_z , δ , and \mathcal{Q} then set them to zero. After some manipulations (see Chandrasekhar (1983) for details), one can find that the equation governing the motion of the photon ($\delta = 0$) in r and θ is

$$\int^r \frac{dr}{\sqrt{R(r, \xi, \eta)}} = \int^\theta \frac{d\theta}{\sqrt{\Theta(\theta, \xi, \eta)}} = P, \quad (7)$$

where

$$R(r, \xi, \eta) = r^4 + (a^2 - \xi^2 - \eta) r^2 + 2M (\eta + (\xi - a)^2) r - a^2 \eta, \quad (8)$$

$$\Theta(\theta, \xi, \eta) = \eta + a^2 \cos^2 \theta - \xi^2 \cot^2 \theta, \quad (9)$$

and P is the parameter along the photon trajectory. Here we have defined two dimensionless impact parameters $\xi = L_z/E$ and $\eta = \mathcal{Q}/E^2$. The equations of motion for other coordinates (including the affine parameter λ) can be expressed as combinations of the integrals about r and θ

$$\lambda = \int^r \frac{r^2 dr}{\sqrt{R(r, \xi, \eta)}} + \int^\theta \frac{a^2 \cos^2 \theta d\theta}{\sqrt{\Theta(\theta, \xi, \eta)}}, \quad (10)$$

$$t = E\lambda + 2M \int^r r (Er^2 - aL_z + a^2 E) \frac{dr}{\Delta \sqrt{R(r, \xi, \eta)}}, \quad (11)$$

$$\phi = a \int^r ((r^2 + a^2)E - aL_z) \frac{dr}{\Delta \sqrt{R(r, \xi, \eta)}} + \int^\theta (L_z \csc^2 \theta - aE) \frac{d\theta}{\sqrt{\Theta(\theta, \xi, \eta)}}. \quad (12)$$

The upper and lower limits in the integrals about r and θ correspond to the turning points of the photon trajectories which are the roots of quartic Eqs. 8 and 9 with different choices of the impact parameters. The limits are not written explicitly here due to the complexity (see Appendix A in Rauch & Blandford (1994) and Tables in Dexter & Agol (2009) for details). Eqs. 7, 10, 11, and 12 are elliptical integrals, which can be reduced to the Carlson's standard forms, then be evaluated numerically by the subroutines provided in Press et al. (1992). In the calculation of photon trajectories, we use the efficient subroutine **geokerr** created by Dexter & Agol (2009) which has integrated the necessary elements described above, to calculate all geodesic coordinates semi-analytically. In addition we shoot photons from the observer's plane of the sky backwards towards the central black hole and search for the intersections of the photons with the disk. This is a more efficient way than tracing the photons from the disk to the observer in our application.

3. Geometric and kinematic structure of the warped accretion disk

3.1. Geometric structure of the disk

In our calculations, we use a series of concentric rings with increasing radii to describe the shape of the geometrically thin warped disk. The spherical (r, θ, ϕ) and cylindrical coordinate system (ρ, ϕ, h) are both appeared in our calculations, and they can be transformed from each other by

$$\begin{aligned} h &= r \sin \beta \cos \varphi \\ &= \rho \tan \beta \cos \psi, \end{aligned} \quad (13)$$

and

$$\begin{aligned} \rho &= r (1 - \sin^2 \beta \cos^2 \varphi)^{1/2} \\ &= r \left(1 - \frac{\sin^2 \beta}{1 + \tan^2 \psi \cos^2 \beta} \right), \end{aligned} \quad (14)$$

where we use $\rho \cos \psi = r \cos \varphi \cos \beta$, $\tan \varphi = \tan \psi \tan \beta$ and $\psi = \phi - \gamma$ in the derivation above. The formalism of the warped disk has been discussed by Terquem & Bertout (1993); Hartnoll & Blackman (2000); Wu et al.

However we assume that the tiled angle is small so that Eq. 17 is a good approximation for the warped disk. For the clarity in this paper, we simply list the 4-velocity of particles below and relegate the detailed derivation to Appendix A.

$$u^0 = \left(\Sigma \Delta A^{-1} - \sin^2 \theta A \Sigma^{-1} \left(\dot{\phi} - \omega \right)^2 - \Sigma \dot{\theta}^2 \right)^{-1/2}, \quad (18)$$

$$u^r = 0, \quad (19)$$

$$u^\theta = \dot{\theta} u^0 = \Omega u^0 (-\cos \psi \cos \beta \sin \varphi \cos \theta + \sin \psi \cos \varphi \cos \theta + \sin \beta \sin \varphi \sin \theta), \quad (20)$$

$$u^\phi = \dot{\phi} u^0 = \frac{\Omega u^0}{\sin \theta} (\sin \psi \cos \beta \sin \varphi + \cos \psi \cos \varphi). \quad (21)$$

4. Emission line profiles and warped disk images

4.1. Emission line profiles

The emission line profile produced by an accretion disk around a black hole is influenced by Doppler shift, gravitational red-shift, beaming effect, and gravitational lensing effect. The changing of photon energy along a bundle of photon trajectories (geodesic congruence) can be characterized by the ratio g of the energy E_{obs} measured by a local inertial (rest) observer at asymptotic infinity to the emitted energy E_{em} measured by an observer comoving with the plasma element on the accretion disk,

$$g = \frac{E_{\text{obs}}}{E_{\text{em}}} = \frac{(u^\mu p_\mu)_{\text{obs}}}{(u^\mu p_\mu)_{\text{em}}} = (1+z)^{-1}, \quad (22)$$

where $z \equiv (\lambda_{\text{obs}} - \lambda_{\text{em}})/\lambda_{\text{em}}$ is the red-shift as usually defined, u^μ in the denominator and numerator are the four-velocity of the emitting plasma element and the observer at infinity respectively, and p_μ is the four-momentum of the photon which propagates from the plasma element to the observer along a null geodesic. The total observed flux F_{obs} is determined by integrating the specific flux dF_{obs} over all the plasma elements on the accreting disk. For the line profile, the specific flux $dF_{\text{obs}}(E_{\text{obs}})$ at observed energy E_{obs} can be expressed as:

$$dF_{\text{obs}}(E_{\text{obs}}) = I_{\text{obs}}(E_{\text{obs}}) d\Omega_{\text{obs}}, \quad (23)$$

where I_{obs} is the observed specific intensity and $d\Omega_{\text{obs}}$ is the observed solid angle subtended by each plasma element. Using Liouville's theorem

$$I_{\text{obs}}/\nu_{\text{obs}}^3 = I_{\text{em}}/\nu_{\text{em}}^3 \quad (24)$$

we find

$$I_{\text{obs}} = I_{\text{em}} \nu_{\text{obs}}^3 / \nu_{\text{em}}^3 = I_{\text{em}} g^3 = I_{\text{em}} (1+z)^{-3}. \quad (25)$$

And the observed solid angle $d\Omega_{\text{obs}}$ is naturally the size of the pixels in the observer's screen. The detailed derivation of the factor g for the warped disk is shown in Appendix A. We ignore the intrinsic line width and assume $I_{\text{em}} = \varepsilon \delta(E_{\text{em}} - E_0)$, where E_0 is the rest energy of photons, $\varepsilon \sim (r/M)^q$ is the surface emissivity, and q is the emissivity index (Fabian et al. 1989).

In the actual computation, we trace every null geodesic from the observer's screen backwards towards the central black hole and search for the interactions of the trajectories with the surface of the disk. The shadowing from the observer due to the warping of the disk is taken into account; we ignore the shadowing from the coronae, since in our calculation we assume that the scale height of the coronae is large compared to

the size of the disk of our interest, therefore this shadowing may not be important. We calculate the observed specific flux dF_{obs} from each plasma element, and add its contribution into a energy bin according to the observed energy of photons ($E_{\text{obs}} = gE_{\text{em}}$). Then we can obtain a line profile by plotting count number ($dF_{\text{bin}}/E_{\text{bin}}$) versus E_{bin} . The number of bins we choose determines the spectrum resolution. We assume an optically thick disk, thus we consider only the direct photons and neglect the photons which would circular around the black hole and strike the disk.

4.1.1. Changing of the spin parameter a

The overall properties of the line profiles can be understood by carefully examining the contribution of the specific flux from each of the narrow rings of the disk, they are determined by the spin parameter, the warping parameters, the emissivity index, shadowing and orientation of the disk relative to a distant observer (both the inclination angle and azimuthal angle).

Figure 2 shows the line profiles from the warped accretion disk with the warping parameters $n_1 = 0$, $n_2 = 1$, and $n_3 = 0.95$. The inner radius r_{in} of the prograde disk ($\epsilon = 1$) locates at the innermost stable circular orbit (ISCO), which is $4.23 r_g$ for the black hole spin parameter $a = 0.5M$ (maybe a good estimate for the supermassive black hole in Sgr A*). The outer radius is chosen as $r_{\text{out}} = 50 r_g$. From Eq. 16 we know that the tilt angles are 0° and 54° for the narrow rings of the disk at the inner radius and the outer radius respectively. This warped disk is twist-free which means that the twist angle γ does not depend on the radius ($n_1 = 0$). The emissivity index q is taken to be -2 . The horizontal axis is the g factor, i.e. the observed photon energy per unit iron K-shell photon energy, while the vertical axis gives flux in arbitrary units at different observed photon energies. In each panel, there are three colored line profiles representing the inclination angles θ of 10° (red), 50° (blue), and 70° (black) measured from the spin axis of the black hole respectively. Panels (a)-(h) contain the line profiles seen from different azimuthal viewing angles, for the retrograde precession of the warped disk about the spin axis of the black hole from 0° to 315° with uniform angular intervals of 45° . Panel (a) shows the $\phi = 0^\circ$ case, which is defined as the observer viewing from the direction furthest from the lowest point of the disk. Panel (i) shows the line profiles from the standard flat disk with the same inner and outer radius for comparison.

The line profile is sensitive to the inclination angle of the observer. For the low inclination angle $\theta = 10^\circ$ (red), the line profile in panels (a)-(h) tends to be a single broad peak with the same endpoints of the red and blue tails, and almost all of the photons are red-shifted due to strong gravitational red-shift and weak Doppler blue-shift. Those line profiles are similar to the flat disk line profile in panel (i). With the increase of the inclination angle (blue and black), the two-peak or multi-peak structures start to emerge. Compared with the flat disk case where the two peaks are shown (the blue peak is always brighter than the red one), the line profiles from the warped disk present considerable changing of the features, for example the red peak can be comparable or stronger than the blue one in some cases. The deviations are produced by the warping structure and shadowing effect. which can only be seen from the images of the disk in Fig. 3 (for $\theta = 50^\circ$).

For the large inclination angles ($\theta = 50^\circ$ and $\theta = 70^\circ$), the shape of the line profiles is also sensitive to the azimuthal angle. This is because the observable regions of the disk are changing with the precession of the disk over a long period (see images in Figs. 3 for $\theta = 50^\circ$). It appears that the line profiles are less sensitive to the low inclination angles ($\theta = 10^\circ$). Since at the low inclination, the inner region of the disk is almost face-on (for the twist-free warped disk the innermost area coincides with the equatorial plane) and

the shadowing effect due to the warping is less important. We note that the black lines in panel (a) ($\phi = 0^\circ$) and panel (e) ($\phi = 180^\circ$) for $\theta = 70^\circ$ are similar, and the relatively narrower tails for $\phi = 0^\circ$ is due to the fact that part of the strongly blue-shifted and red-shifted area is shadowed.

Figure 4 shows the line profiles from the accretion disk with the same warping parameters n_1 , n_2 , and n_3 as in Figure 2 but for a more relativistic system, where the black hole has an extreme spin parameter $a = 0.998M$ (Thorne 1974). The inner radius r_{in} for the accretion disk is only $1.23 r_g$. The general features mentioned for Figure 2 hold here. In addition, the effect of the gravitational red-shift and light bending is more significant. Some photon trajectories which are initially retrograde may be forced to turn back to be prograde by the frame dragging effect. In this more relativistic system, the red tails are rather long and extend to as far as $g = 0.1$, while the blue tails end at about the same places as in Figure 2, although they are cut off more sharply for largest inclinations ($\theta = 70^\circ$). However, the line profiles around $g = 1$ (the rest energy) are very similar to Figure 2, since the contribution to the flux here is mainly from the rings in the outer region of the disk ($r > 10 r_g$), where the frame dragging effect is much smaller ($w \propto r^{-3}$).

Figure 5 shows the line profiles from the accretion disk with the same warping and spin parameters as in Figures 2, except we choose the disk to rotate around the black hole in a retrograde orbit ($\epsilon = -1$). The retrograde orbiting of the disk will increase its inner radius r_{in} to a larger value $7.55 r_g$, which reduces the contribution from the innermost part of the disk so that the red and blue tails become slimmer than in Fig. 2. In addition the patterns are anti-symmetric about 180° compared to Fig. 2.

4.1.2. Changing of the emissivity index q

The detailed irradiation law is unknown and the emissivity of the iron line in the inner region of the disk is poorly understood so far. For simplicity, we assume that the emissivity is a power-law function of radius with the emissivity index as the power-law index (i.e. $\varepsilon \sim (r/M)^q$).

Figure 6 shows the line profiles from the warped disk with the same warping parameters and the spin parameter as in Figure 2. The difference is that the inclination angle θ in all cases here are chosen as 70° measured from the black hole spin axis. In each panel, the three colored lines represent the line profiles with the emissivity index q being -2 (red), -2.5 (blue), and -3 (black) respectively. Panels (a)-(h) contain the line profiles seen from different azimuthal viewing angles as in Figs. 2–5, and panel (i) shows the line profiles from the standard flat disk for comparison. All the line profiles are normalized to unity.

Generally speaking, smaller emissivity index indicates relatively larger contribution from the inner region of the disk, if we do not consider the shadowing effect which prevents part of the inner region to be seen in some cases. The inner regions contribute mostly to the flux at blue and red tails while the outer region to that around $g = 1$ (the rest energy). Therefore, for smaller emissivity index (black than red), the flux in the red/blue tails is more intensive than that for larger emissivity index. However the shadowing effect is pronounced in some cases. For example in panel (a) ($\phi = 0^\circ$), part of the most blue-shifted region is unobservable due to the shadowing, the blue tails for three different q are almost identical. Moreover, they are less blue-shifted ($g \simeq 1.2$) and are not steep as others. Similar feature appears in panel (b) ($\phi = 45^\circ$) and panel (h) ($\phi = 315^\circ$) too. In panel (e) ($\phi = 180^\circ$), the disk is fully observed (least shadowing), the main feature of the line profile is similar to the flat disk where there is no shadowing at all. In panels (c)–(g), where the shadowing effect is less important, the blue tails for smaller emissivity index are steeper, and it is a common feature shared by both the warped disk and the flat disk. Since the nature of the central black hole, the dynamic structure of the disk and the orientation to the observer are the same for profiles in each

panel, the blue and red tails representing different emissivity index end at the same places.

Figure 7 shows the line profiles from the warped disk with the same warping parameter and the spin parameter as in Figure 6, but the inclination angle θ here are chosen as 50° . The features mentioned for Figure 6 remain true here. Furthermore the blue tails are reduced to smaller values ($g < 1.2$) and cut off more steeply due to smaller Doppler blue-shift for this smaller inclination angle; while the red tails end at about the same value ($g \simeq 0.4$), because they are mainly from the gravitational red-shift which is not sensitive to the inclination angle.

Figure 8 shows the line profiles from the warped disk with the same warping parameter and inclination angle as in Figure 7 but with the spin parameter $a = 0.998M$. For such extreme spin rate, the inner radius of the accretion disk can be very close to the event horizon ($r_h = 1.0632 r_g$), where the gravitational red-shift dominates. Therefore the red tails in Figure 8 are much longer than those in Figure 7. For the reason we motioned above, smaller emissivity index usually produces more intensive red tails, the red tails for $q = -3$ (black) is stronger than those of the other two lines. In extreme case, for example panel (a), a bump appears in the red tail of $q = -3$.

5. Discussion and Conclusions

To date there are two practical methods for measuring the spin of astrophysical black holes, namely the X-ray continuum fitting and the relativistic iron lines. The continuum-fitting method so far can only be applied to stellar-mass black holes (McClintock et al. 2011), whereas the relativistic iron lines can be used as a probe to both the spins of stellar-mass black holes in X-ray binaries and supermassive black holes in active galactic nuclei. Furthermore if the accretion disks in these systems are warped, it is possible that the relativistic iron line profiles may serve as a way to diagnose the structures of the disks.

In this paper we have developed a method for calculating the emission line profiles from the warped accretion disks orbiting around rotating black holes. It essentially generalizes previous calculations by including the black hole spin, the disk warping and the shadowing effect at the same time. We have also presented the disk images which can help us understand the general features of the line profiles from different disk and black hole systems. The detailed calculation concerns the computation of the trajectories of the photons emitted from the disk and the velocity field of the plasma elements orbiting around the center black hole. The formalism described above makes no assumption about the emitting energy of the photon. Therefore it can be applied to any emission lines which could be detected in the immediate vicinity of the black hole, such as the carbon, nitrogen, and oxygen lines although they are not as prominent as the iron lines.

We assumed a set of warping parameters for the geometry of the twist-free warping disk and Keplerian orbit for the motion of the plasma elements as examples. Even for this simplified system we have found a number of interesting phenomena: (1) Different from the two-peak feature generally found in flat disks, the line profiles from the warped disk show multiple peaks. (2) The line profiles for some cases present sharper red tails and/or softer blue tails, which may provide an alternative explanation to observations for some Seyfert 1 galaxies (Nandra et al. 1997) and Seyfert 2 galaxies (Turner et al. 1997). (3) When the disks are orbiting around a highly spinning black hole, a rather long red tail is a common feature shared between flat disks and warped disks, if the shadowing effect is not important. (4) At low inclinations, the line profiles from different azimuthal angles differ very little from each other, indicating that the warping has little influence on the line profile and it may not provide much information for diagnosing the disk structure. (5) The line

profile is also sensitive to the illumination law: smaller emissivity index q generally indicates stronger red and blue tails. In some extreme cases, red bumps may grow in the red tails. (6) It may not be true that a sharp blue tail is a common feature in all axisymmetric disk models, and is expected for time-integrated profiles even if the disk has strong asymmetry or inhomogeneities (Bromley et al. 1998). The shadowing we encounter here may cause a soft blue tail in the integrated profile. (7) With the precession of the warped disk, time variations of line profiles may be present, and may be a possible observational signature for the warped disk. (8) Photometric variations of the line fluxes may be due to the varying amount of area of the disk facing to the observer.

It is nontrivial to constrain the model parameters by fitting the theoretical line profiles to observations. However, from the above results and discussions we can see that generally the red tails of the line profiles provide the information about the spin of the black hole, while the blue tails the inclination angle. And the warping would cause complicated multiple peaks (which depends on the warping parameters), and time-variation of line profiles with the precession of disk. In the large inclination cases, the warping would cause significant disk shadowing which may prevent all/part of the inner area to be seen. Smaller emissivity index q normally indicates more intensive red and blue tails in the line profiles. Our present work is an initiative of a systematic investigation about the impact of the disk warping and shadowing on the line profile. It can be considered as an extension of previous work on line profiles for warped disk (Hartnoll & Blackman 2000; Wu et al. 2008). Our line profiles distinguish from the line profiles from non-rotating black hole systems by presenting longer red tails which could extend to $g = 0.1$ for highly spinning cases. And the overall line feature is smooth and has similarity to the flat disk if the shadowing is not significant. These are different from Hartnoll & Blackman (2000), in which there are abrupt spike-like structures in some cases. We provide an alternative explanation to the variation of line profile which is complementary to the picture of Karas et al. (2001), who investigate the non-axisymmetric patterns in the disk surface. However the non-axisymmetric patterns are unlikely to produce multiple peak structure. Due to the axisymmetry, both the thick disk (Wu & Wang 2007) and accretion torus (Fuerst & Wu 2007) would not show the time-variant of line profile with the precession and the line profiles are usually single-peaked and double-peaked.

Long-period photometric variation of X-ray is observed for many accreting systems. The precession of warped disk may be an explanation for this phenomenon. The time-scale characterizing the precession induced by tidal force of the companion star in XRB (Wijers & Pringle 1999) is

$$t_{\Omega_p} = \frac{2\pi}{\Omega_p} = 6.7 \left(\frac{P_{orb}}{1d} \right)^2 \left(\frac{1+q}{q} \right) \left(\frac{M}{1M_{\odot}} \right)^{1/2} \left(\frac{R}{10^{11}\text{cm}} \right)^{-3/2} d, \quad (26)$$

where P_{orb} is the orbital period of the binary, and q is the ratio of the mass of the companion star to the central accreting object. The time-scale characterizing the precession induced by radiation can be found in Maloney et al. (1996). The typical precession period for an AGN may be much longer than that of the XRB. The purpose of showing this formula is to point out that apart from the time-averaged line profile (with typical explosion time longer than 10^6 s), it is possible to study the time variation of the iron line profiles on the precession timescale with the next generation space X-ray observatories which have sufficiently large collecting area.

With the advance of the millimeter/sub-millimeter very-long baseline interferometer (VLBI), the proposed Earth-based *Event Horizon Telescope* (EHT) (Doeleman et al. 2009) and the on-going space-VLBI

(such as VSOP¹ and RadioAstron²) promise to provide microarcsecond imaging resolution, which is sufficient to resolve the event horizons and the inner regions of the accretion disks around a handful of super-massive black holes. The calculated disk images may help understand the possible asymmetric intensity profile, blue/red-shift, and other observational signatures caused by the warping of the accretion disk and the rotating of the black hole. In the following work we will try to constrain the model parameters by fitting the theoretical profiles of the predicted spectra to actual data.

Although we have given results for only one set of warping parameters, our formalism can be easily extended to more general disks. Work is underway on investigating systems with different warping parameters. By using the method of moments, we can explore the large warping parameter space (n_1, n_2, n_3) and study the distribution of the warping parameters in the moment space. In practice, it may be helpful to compare the positions of the prominent line peaks in the warped disks with the corresponding peaks in the flat disks. And it would be easier than fitting the overall line profiles (Murphy et al. 2009; Sochora et al. 2011). Through this approaches we may connect the calculated line profiles with the current and/or future observations.

6. Acknowledgment

We are grateful to an anonymous referee for constructive comments. We also thank Xinlian Luo, Teviet Creighton and Frederick Jenet for helpful discussions and comments, and Richard Price for directing us to several related publications and reviewing the manuscript. This work was supported by the Natural Science Foundation of China (under grant number 10873008), and the National Basic Research Program of China (973 Program 2009CB824800).

A. Expression of g for the warped disks

This section describes how to derive the expression of g , the ratio of observed photon energy to the emitted energy for the warped disk.

A.1. 4-velocity of the particle

In each concentric ring, we let the angular position of the each plasma element be $\varphi = \Omega t$, with t the coordinate time in the Kerr metric and the plasma particle's velocity components are

$$\mathbf{v}' = dx'/dt = v(-\sin\varphi, \cos\varphi, 0), \quad (\text{A1})$$

where $v = r\Omega = r(a + \epsilon\sqrt{r^3/M})^{-1}$, $\epsilon = 1$ is for co-rotating/prograde orbiting, $\epsilon = -1$ is for counter-rotating/retrograde orbiting. In addition, we need to transfer the velocity into the coordinate frame in which the z axis is aligned with the black hole spin. In Figure 1, the inclined $x'y'$ plane is the orbital plane, and the y' axis coincides with the line of nodes and points at the ascending node. The xy plane is the equatorial plane which has a tilt angle β relative to the $x'y'$ plane. The projection of the z' axis on the xy

¹<http://www.vsop.isas.ac.jp/>

²<http://www.asc.rssi.ru/radioastron/>

plane has a twist angle γ relative to the x axis. We find the components v_i in the xyz coordinate basis using $v_i = T_{ij'} v_{j'}$, where

$$T_{ij'} = \begin{pmatrix} \cos \gamma \cos \beta & -\sin \gamma & -\cos \gamma \sin \beta \\ \sin \gamma \cos \beta & \cos \gamma & -\sin \gamma \sin \beta \\ \sin \beta & 0 & \cos \beta \end{pmatrix}, \quad (\text{A2})$$

from which we get

$$\begin{aligned} v_x &= v (-\cos \gamma \cos \beta \sin \varphi - \sin \gamma \cos \varphi) \\ v_y &= v (-\sin \gamma \cos \beta \sin \varphi + \cos \gamma \cos \varphi) \\ v_z &= v (-\sin \beta \sin \varphi). \end{aligned} \quad (\text{A3})$$

We then calculate the velocity components in the spherical coordinate by projecting the velocity \mathbf{v} onto the spherical basis $\mathbf{e}_r, \mathbf{e}_\theta, \mathbf{e}_\phi$

$$\begin{aligned} v_r &= 0 \\ v_\theta &= v (-\cos \psi \cos \beta \sin \varphi \cos \theta + \sin \psi \cos \varphi \cos \theta + \sin \beta \sin \varphi \sin \theta) \\ v_\phi &= v (\sin \psi \cos \beta \sin \varphi + \cos \psi \cos \varphi). \end{aligned} \quad (\text{A4})$$

where $\psi = \phi - \gamma$ is the azimuthal angle of the plasma element measured from the projection of the x' axis on the xy plane.

In the Kerr spacetime, if we set τ as the proper time of the plasma element, it satisfies

$$-d\tau^2 = ds^2 = -\Sigma \Delta A^{-1} dt^2 + \sin^2 \theta A \Sigma^{-1} (d\phi - \omega dt)^2 + \Sigma \Delta^{-1} dr^2 + \Sigma d\theta^2, \quad (\text{A5})$$

and we divide both sides by dt^2

$$-\frac{d\tau^2}{dt^2} = -\Sigma \Delta A^{-1} + \sin^2 \theta A \Sigma^{-1} (\dot{\phi} - \omega)^2 + \Sigma \dot{\theta}^2. \quad (\text{A6})$$

Therefore we can write the 4-velocity of the plasma element as follow,

$$\begin{aligned} u^0 &= \frac{dt}{d\tau} = \left(\Sigma \Delta A^{-1} - \sin^2 \theta A \Sigma^{-1} (\dot{\phi} - \omega)^2 - \Sigma \dot{\theta}^2 \right)^{-1/2} \\ u^r &= \frac{dr}{d\tau} = \frac{dr}{dt} \frac{dt}{d\tau} = \dot{r} u^0 = 0 \\ u^\theta &= \frac{d\theta}{d\tau} = \frac{d\theta}{dt} \frac{dt}{d\tau} = \dot{\theta} u^0 = u^0 \frac{v_\theta}{r} \\ u^\phi &= \frac{d\phi}{d\tau} = \frac{d\phi}{dt} \frac{dt}{d\tau} = \dot{\phi} u^0 = u^0 \frac{v_\phi}{r \sin \theta}. \end{aligned} \quad (\text{A7})$$

which are identical to Eq. 18 in Sec. 3.2 if insert Eq. A4 into Eq. A7. We note that the radial component of the velocity is zero because of we have assumed that the particle follows Keplerian orbit. And the term under the square root of Eq. A7 is always positive if $r > r_{\text{ISCO}}$.

A.2. expression for g

The 4-velocity of the particle are expressed by the Boyer-Lindquist coordinates in Eq. A7, we then derive the expression for g . As defined

$$g = \frac{E_{\text{obs}}}{E_{\text{em}}} = \frac{(u^\mu p_\mu)_{\text{obs}}}{(u^\mu p_\mu)_{\text{em}}} = (1+z)^{-1}. \quad (\text{A8})$$

The observer rest at infinity has 4-velocity $p_\mu=(-1, 0, 0, 0)$, thus in the numerator $(u^\mu p_\mu)_{\text{obs}} = E$; while in the denominator

$$(u^\mu p_\mu)_{\text{em}} = -Eu^0 \pm Eu^0 \sqrt{\Theta} v_\theta / r + L_z u^0 v_\phi / \sin \theta , \quad (\text{A9})$$

therefore we get

$$g = \frac{1}{u^0(-1 \pm \sqrt{\Theta} v_\theta / r + \xi v_\phi / \sin \theta)} , \quad (\text{A10})$$

where the sign is determined by the zenithal emitting direction.

REFERENCES

- Abramowicz, M. A., Jaroszyński, M., Kato, S., Lasota, J., Różańska, A., & Sądowski, A. 2010, *A&A*, 521, A15+
- Bardeen, J. M., & Petterson, J. A. 1975, *ApJ*, 195, L65+
- Barr, P., White, N. E., & Page, C. G. 1985, *MNRAS*, 216, 65P
- Brenneman, L. W., & Reynolds, C. S. 2006, *ApJ*, 652, 1028
- Bromley, B. C., Chen, K., & Miller, W. A. 1997, *ApJ*, 475, 57
- Bromley, B. C., Miller, W. A., & Pariev, V. I. 1998, *Nature*, 391, 54
- Carter, B. 1968, *Physical Review*, 174, 1559
- Chandrasekhar, S. 1983, *The mathematical theory of black holes*, ed. Chandrasekhar, S.
- Demianski, M., & Ivanov, P. B. 1997, *A&A*, 324, 829
- Dexter, J., & Agol, E. 2009, *ApJ*, 696, 1616
- Doeleman, S., Agol, E., Backer, D., Baganoff, F., Bower, G. C., Broderick, A., Fabian, A., Fish, V., Gammie, C., Ho, P., Honman, M., Krichbaum, T., Loeb, A., Marrone, D., Reid, M., Rogers, A., Shapiro, I., Strittmatter, P., Tilanus, R., Weintraub, J., Whitney, A., Wright, M., & Ziurys, L. 2009, in *ArXiv Astrophysics e-prints*, Vol. 2010, astro2010: The Astronomy and Astrophysics Decadal Survey, 68–+
- Fabian, A. C., Rees, M. J., Stella, L., & White, N. E. 1989, *MNRAS*, 238, 729
- Fanton, C., Calvani, M., de Felice, F., & Cadez, A. 1997, *PASJ*, 49, 159
- Frank, J., King, A., & Raine, D. J. 2002, *Accretion Power in Astrophysics: Third Edition*
- Fuerst, S. V., & Wu, K. 2007, *A&A*, 474, 55
- Hartnoll, S. A., & Blackman, E. G. 2000, *MNRAS*, 317, 880
- . 2002, *MNRAS*, 332, L1
- Ivanov, P. B., & Illarionov, A. F. 1997, *MNRAS*, 285, 394
- Karas, V., Martocchia, A., & Subr, L. 2001, *PASJ*, 53, 189

- Katz, J. I. 1973, *Nature*, 246, 87
- Kinney, A. L., Schmitt, H. R., Clarke, C. J., Pringle, J. E., Ulvestad, J. S., & Antonucci, R. R. J. 2000, *ApJ*, 537, 152
- Laor, A. 1991, *ApJ*, 376, 90
- Larwood, J. D., Nelson, R. P., Papaloizou, J. C. B., & Terquem, C. 1996, *MNRAS*, 282, 597
- Lubow, S. H., Ogilvie, G. I., & Pringle, J. E. 2002, *MNRAS*, 337, 706
- Maloney, P. R., Begelman, M. C., & Nowak, M. A. 1998, *ApJ*, 504, 77
- Maloney, P. R., Begelman, M. C., & Pringle, J. E. 1996, *ApJ*, 472, 582
- Margon, B. 1984, *ARA&A*, 22, 507
- Martin, R. G. 2008, *MNRAS*, 387, 830
- Matt, G., Perola, G. C., & Piro, L. 1991, *A&A*, 247, 25
- McClintock, J. E., Narayan, R., Davis, S. W., Gou, L., Kulkarni, A., Orosz, J. A., Penna, R. F., Remillard, R. A., & Steiner, J. F. 2011, *ArXiv e-prints*
- Melia, F. 2007, *The Galactic Supermassive Black Hole* (Princeton University Press)
- Miller, J. M. 2007, *ARA&A*, 45, 441
- Miller, J. M., Fabian, A. C., Wijnands, R., Remillard, R. A., Woźdowski, P., Schulz, N. S., Di Matteo, T., Marshall, H. L., Canizares, C. R., Pooley, D., & Lewin, W. H. G. 2002a, *ApJ*, 578, 348
- Miller, J. M., Fabian, A. C., Wijnands, R., Reynolds, C. S., Ehle, M., Freyberg, M. J., van der Klis, M., Lewin, W. H. G., Sanchez-Fernandez, C., & Castro-Tirado, A. J. 2002b, *ApJ*, 570, L69
- Miniutti, G., Fabian, A. C., Anabuki, N., Crummy, J., Fukazawa, Y., Gallo, L., Haba, Y., Hayashida, K., Holt, S., Kunieda, H., Larsson, J., Markowitz, A., Matsumoto, C., Ohno, M., Reeves, J. N., Takahashi, T., Tanaka, Y., Terashima, Y., Torii, K., Ueda, Y., Ushio, M., Watanabe, S., Yamauchi, M., & Yaqoob, T. 2007, *PASJ*, 59, 315
- Miniutti, G., Fabian, A. C., & Miller, J. M. 2004, *MNRAS*, 351, 466
- Misner, C. W., Thorne, K. S., & Wheeler, J. A. 1973, *Gravitation* (San Francisco: Freeman)
- Miyoshi, M., Moran, J., Herrnstein, J., Greenhill, L., Nakai, N., Diamond, P., & Inoue, M. 1995, *Nature*, 373, 127
- Murphy, K. D., Yaqoob, T., Karas, V., & Dovčiak, M. 2009, *ApJ*, 701, 635
- Nandra, K., George, I. M., Mushotzky, R. F., Turner, T. J., & Yaqoob, T. 1997, *ApJ*, 477, 602
- Novikov, I. D., & Thorne, K. S. 1973, in *Black Holes (Les Astres Occlus)*, ed. C. Dewitt & B. S. Dewitt, 343–450
- Page, D. N., & Thorne, K. S. 1974, *ApJ*, 191, 499

- Press, W. H., Teukolsky, S. A., Vetterling, W. T., & Flannery, B. P. 1992, Numerical recipes in FORTRAN. The art of scientific computing, ed. Press, W. H., Teukolsky, S. A., Vetterling, W. T., & Flannery, B. P.
- Pringle, J. E. 1996, MNRAS, 281, 357
- Rauch, K. P., & Blandford, R. D. 1994, ApJ, 421, 46
- Reynolds, C. S., & Nowak, M. A. 2003, Phys. Rep., 377, 389
- Rossi, S., Homan, J., Miller, J. M., & Belloni, T. 2005, MNRAS, 360, 763
- Schmitt, H. R., Pringle, J. E., Clarke, C. J., & Kinney, A. L. 2002, ApJ, 575, 150
- Shakura, N. I., & Sunyaev, R. A. 1973, A&A, 24, 337
- Sochora, V., Karas, V., Svoboda, J., & Dovčiak, M. 2011, MNRAS, 1522
- Tanaka, Y., Nandra, K., Fabian, A. C., Inoue, H., Otani, C., Dotani, T., Hayashida, K., Iwasawa, K., Kii, T., Kunieda, H., Makino, F., & Matsuoka, M. 1995, Nature, 375, 659
- Tananbaum, H., Gursky, H., Kellogg, E. M., Levinson, R., Schreier, E., & Giacconi, R. 1972, ApJ, 174, L143+
- Terquem, C., & Bertout, C. 1993, A&A, 274, 291
- Thorne, K. S. 1974, ApJ, 191, 507
- Turner, T. J., George, I. M., Nandra, K., & Mushotzky, R. F. 1997, ApJ, 488, 164
- Wijers, R. A. M. J., & Pringle, J. E. 1999, MNRAS, 308, 207
- Wilms, J., Reynolds, C. S., Begelman, M. C., Reeves, J., Molendi, S., Staubert, R., & Kendziorra, E. 2001, MNRAS, 328, L27
- Wu, S., Wang, T., & Dong, X. 2008, MNRAS, 389, 213
- Wu, S.-M., & Wang, T.-G. 2007, MNRAS, 378, 841
- Young, A. J., Ross, R. R., & Fabian, A. C. 1998, MNRAS, 300, L11

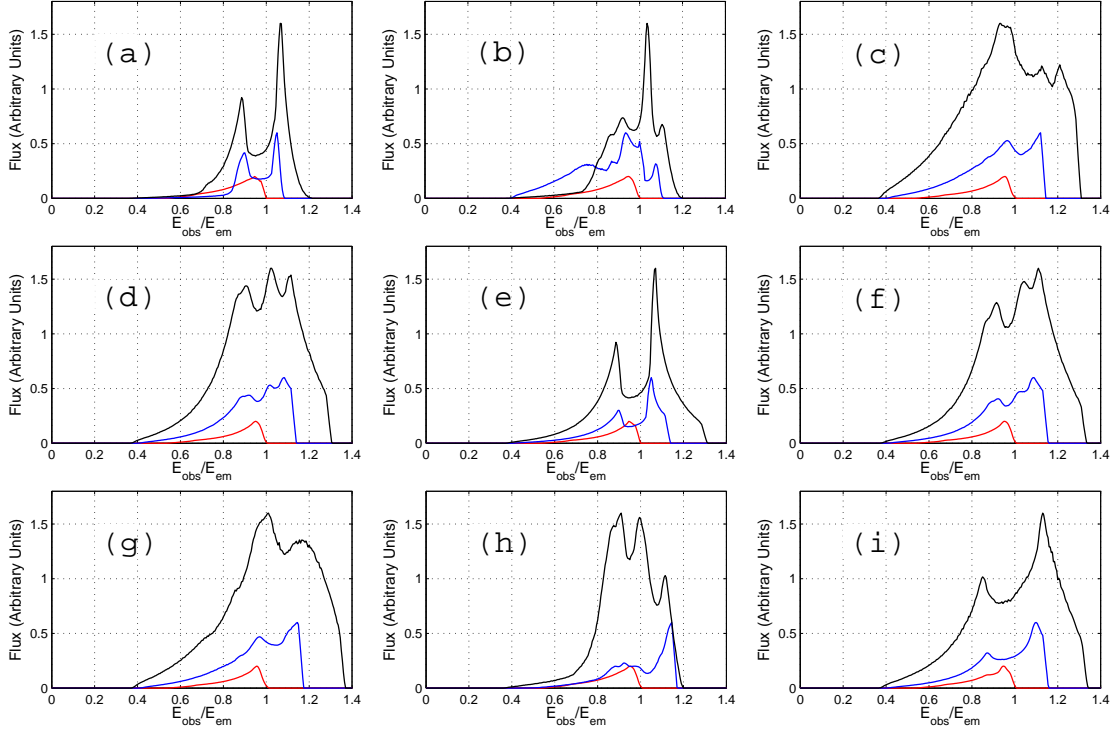


Fig. 2.— Line profiles from a warped disk with $n_1 = 0$, $n_2 = 1$, $n_3 = 0.95$, $r_{\text{in}} = 4.23 r_g$ and $r_{\text{out}} = 50 r_g$. The spin parameter a of the Kerr black hole is $0.5M$. The emissivity index q is taken to be -2 . The horizontal axis is the g factor, i.e. the observed photon energy per unit iron K-shell photon energy; the vertical axis is flux in arbitrary units. In each panel, three colored line profiles represent inclination angles θ of 10° (red), 50° (blue), and 70° (black) measured from the spin axis of the black hole respectively. Panels (a)-(h) contain the line profiles seen from different azimuthal angles ϕ of 0° , 45° , 90° , 135° , 180° , 225° , 270° and 315° . Panel (a) shows the $\phi = 0^\circ$ case which is defined as the observer viewing from the direction furthest from the lowest point of the disk. Panel (i) shows the line profile from a standard flat disk for comparison.

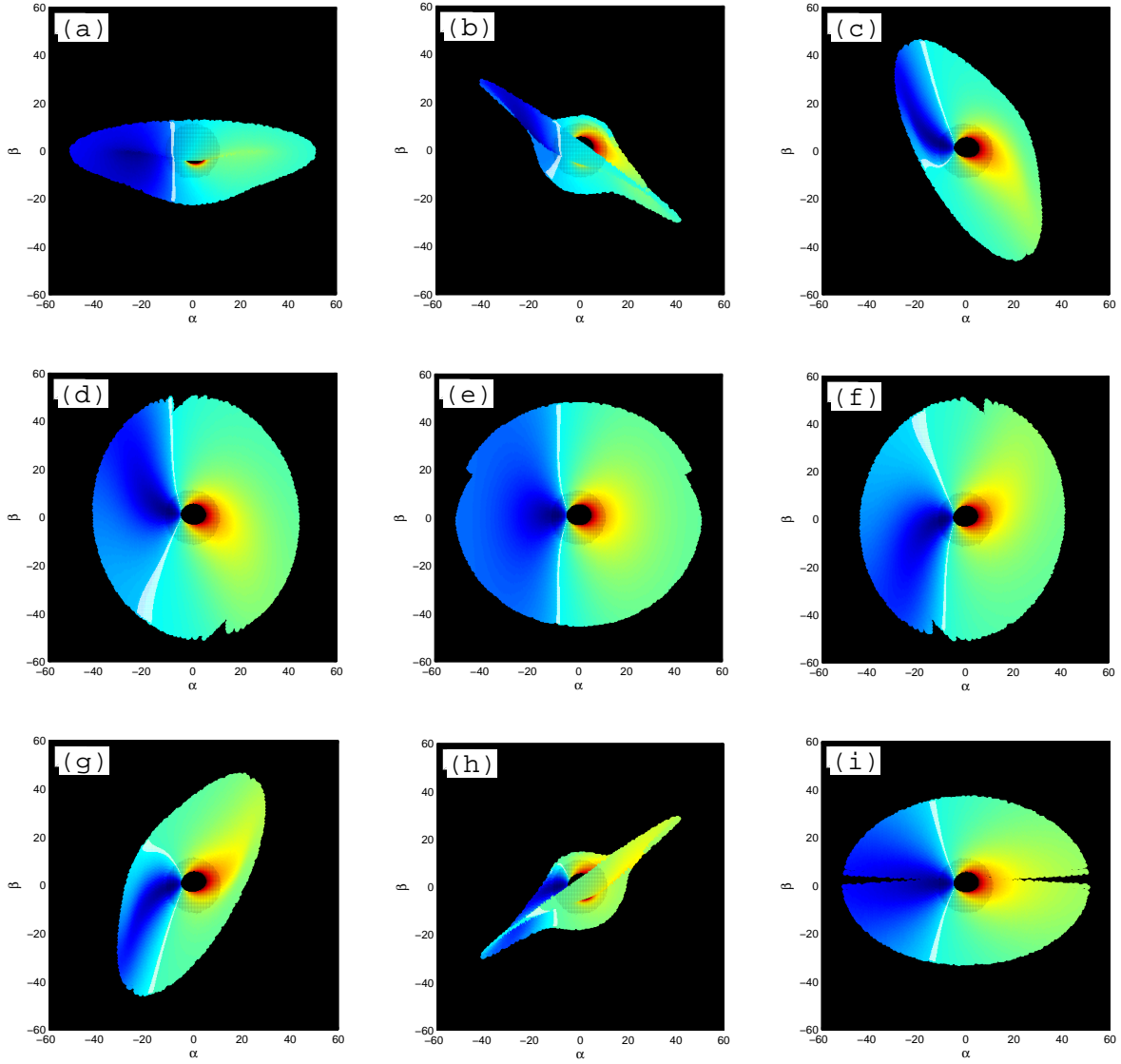


Fig. 3.— Images of a geometrically thin and optically thick warped disk around a Kerr black hole. The spin parameter a is $0.5M$, and the observer’s inclination angle θ is 50° measured from the spin axis. The warping parameters are the same as previous figures ($n_1 = 0$, $n_2 = 1$, $n_3 = 0.95$). The inner and outer radius are $4.23 r_g$ and $50 r_g$. α is the horizontal axis of the observer’s photographic plate, and β is the vertical axis. The false color contour maps show the ratio of the observed energy to the emitted energy. The blue shaded areas represent the regions of the disk where photons emitted are blue-shifted, while the red shaded areas represent the regions where photons are red-shifted. The large areas colored with cyan and green represent the regions where photon energies are weakly blue and red-shifted. The white areas are the zero-shift regions, where the gravitational red-shift is balanced with the Doppler blue-shift. Panels (a)-(h) contain the line profiles seen from different azimuthal angles ϕ of 0° , 45° , 90° , 135° , 180° , 225° , 270° and 315° . Panel (a) shows the $\phi = 0^\circ$ case which is defined as the observer viewing from the direction furthest from the lowest point of the disk. Panel (i) shows the disk image from a standard flat disk for comparison.

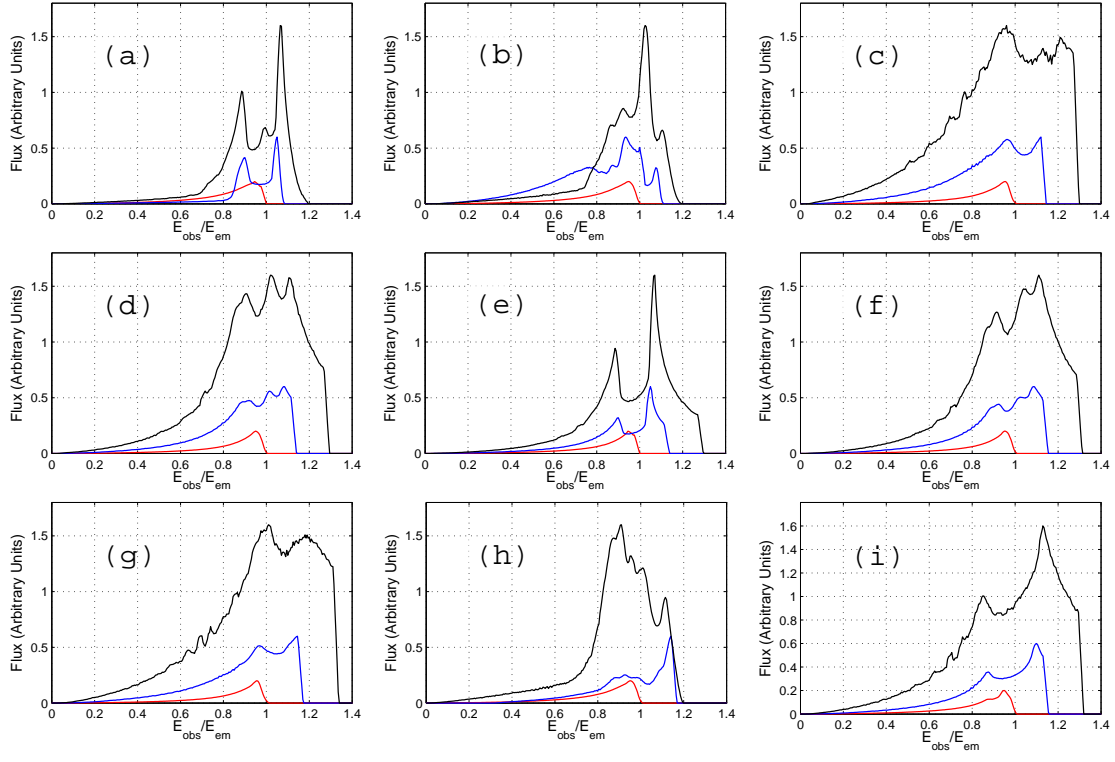


Fig. 4.— Line profiles as in Fig. 2 with $a = 0.998M$, $r_{\text{in}} = 1.23 r_g$ and $r_{\text{out}} = 50 r_g$.

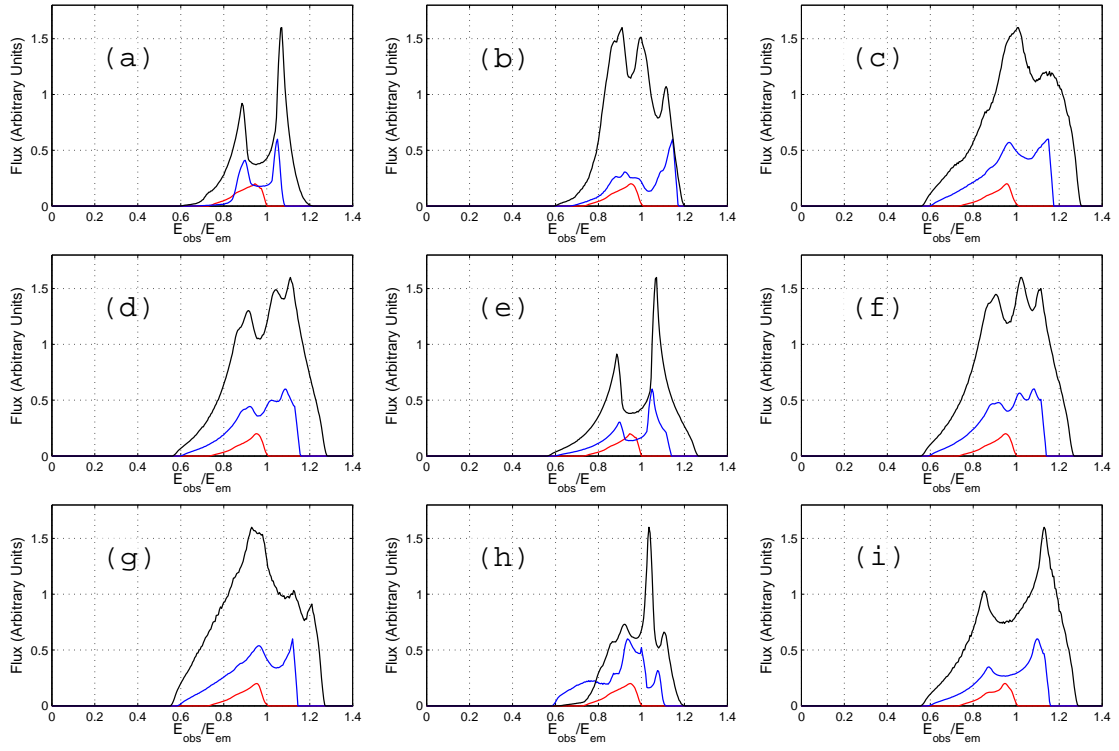


Fig. 5.— Line profiles as in Fig. 2 with $a = -0.5M$, $r_{\text{in}} = 7.55 r_g$ and $r_{\text{out}} = 50 r_g$.

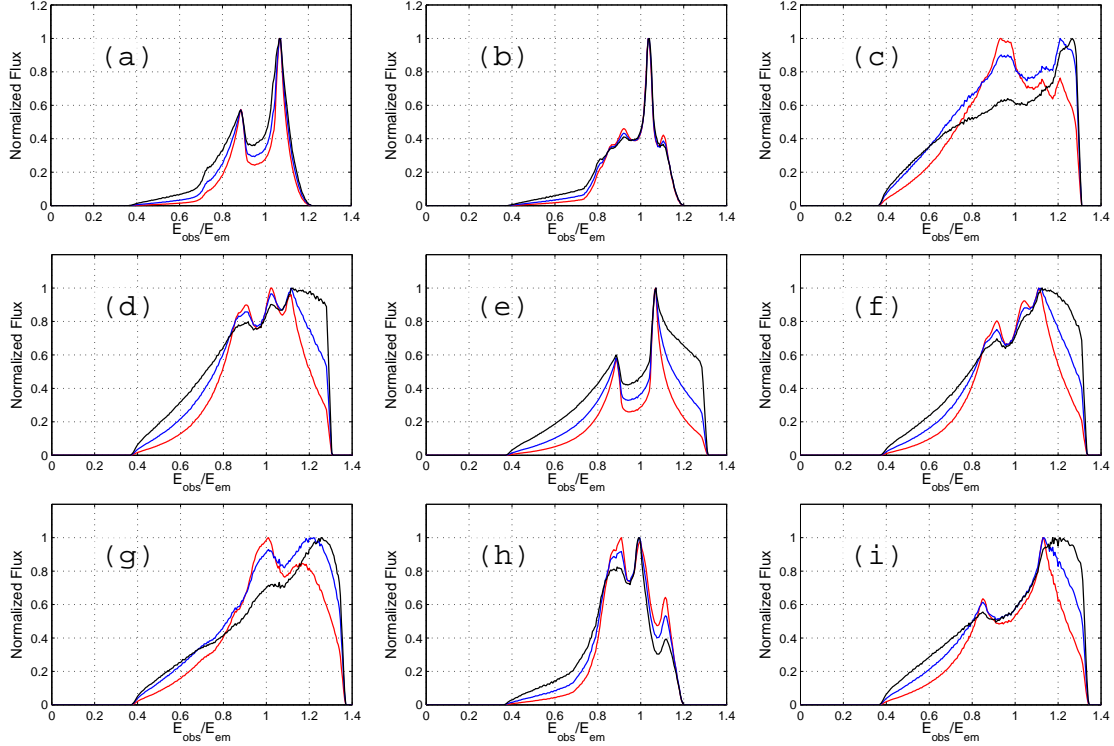


Fig. 6.— Line profiles from a warped disk with $n_1 = 0$, $n_2 = 1$, $n_3 = 0.95$, $r_{\text{in}} = 4.23 r_g$ and $r_{\text{out}} = 50 r_g$. The spin parameter a of the Kerr black hole is $0.5M$. The emissivity index q is taken to be -2 . The horizontal axis is the g factor, i.e. the observed photon energy per unit iron K-shell photon energy; the vertical axis is flux in arbitrary units. The inclination angle θ is 70° measured from the spin axis of the black hole. In each panel, three line profiles represent emissivity index q of -2 (red), -2.5 (blue), and -3 (black) respectively. Panels (a)-(h) contain the line profiles seen from different azimuthal angles ϕ of 0° , 45° , 90° , 135° , 180° , 225° , 270° and 315° . Panel (a) shows the $\phi = 0^\circ$ case which is defined as the observer viewing from the direction furthest from the lowest point of the disk. Panel (i) shows the line profiles from a standard flat disk for comparison.

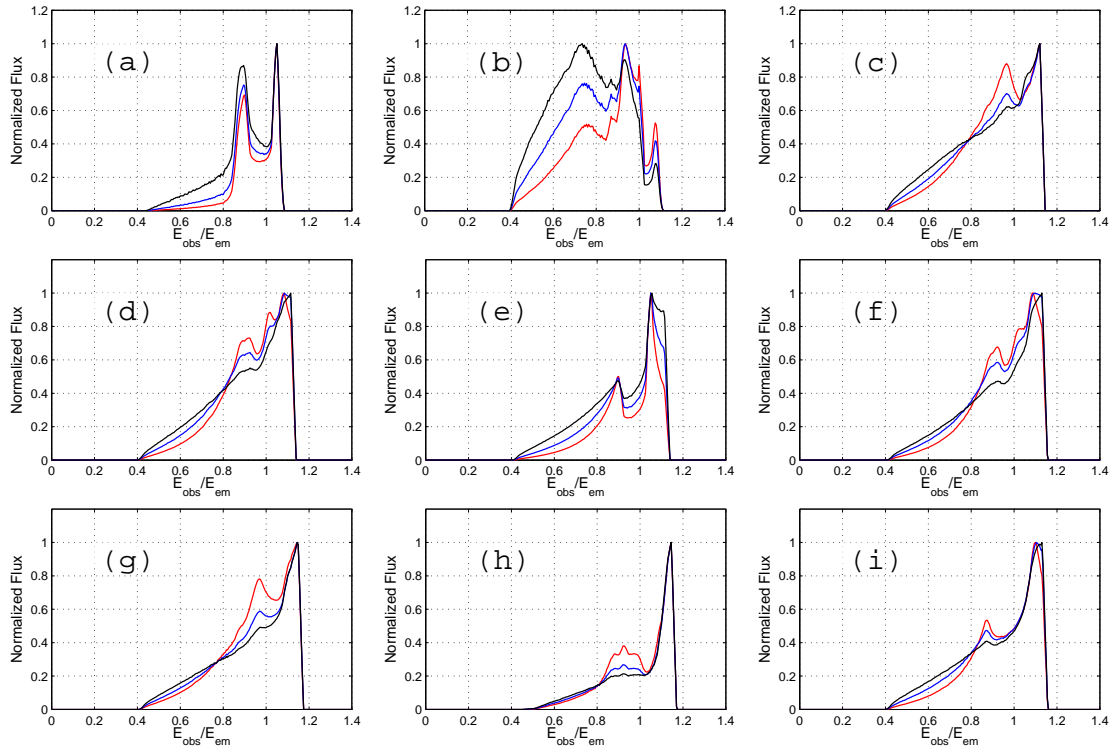


Fig. 7.— Line profiles as in Fig. 6 with $\theta = 50^\circ$, $r_{\text{in}} = 4.23 r_g$ and $r_{\text{out}} = 50 r_g$.

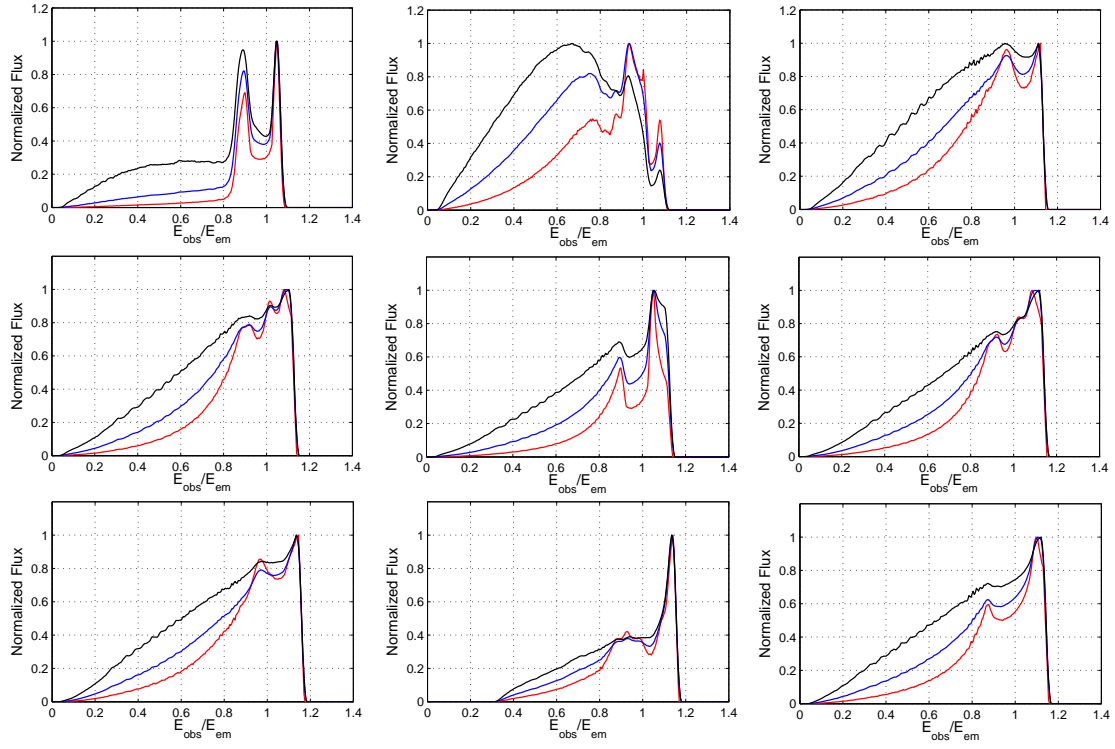


Fig. 8.— Line profiles as in Fig. 7 with $a = 0.998$, $\theta = 50^\circ$, $r_{\text{in}} = 1.23 r_g$ and $r_{\text{out}} = 50 r_g$.